Published in final edited form as:
Biochemistry. 2011 March 1; 50(8): 1403–1411. doi:10.1021/bi101319v.

Use of 2,3,5-F_3Y-β2 and 3-NH_2Y-α2 to study PCET in *E. coli* Ribonucleotide Reductase

Mohammad R. Seyedsayamdost[†,&], **Cyril S. Yee**[†], and **JoAnne Stubbe**[*,†,‡]

[†]Department of Chemistry, Massachusetts Institute of Technology, 77 Massachusetts Avenue, Cambridge, MA 02139–4307

[‡]Department of Biology, Massachusetts Institute of Technology, 77 Massachusetts Avenue, Cambridge, MA 02139–4307

Abstract

E. coli ribonucleotide reductase is an α2β2 complex that catalyzes the conversion of nucleoside 5′-diphosphates (NDPs) to deoxynucleotides (dNDPs). The active site for NDP reduction resides in α2, and the essential diferric-tyrosyl radical (Y_{122}•) cofactor that initiates radical transfer to the active site cysteine in α2 (C_{439}), 35 Å removed, is in β2. The oxidation is proposed to involve a hopping mechanism through aromatic amino acids ($Y_{122}\rightarrow W_{48}\rightarrow Y_{356}$ in β2 to $Y_{731}\rightarrow Y_{730}\rightarrow C_{439}$ in α2) and reversible proton coupled electron transfer (PCET). Recently 2,3,5-F_3Y (F_3Y) was site-specifically incorporated in place of Y_{356} in β2, and 3-NH_2Y (NH_2Y) in place of Y_{731} and Y_{730} in α2. A pH rate profile with F_3Y_{356}-β2 suggested that as the pH is elevated, the rate-determining step of RNR can be altered from a conformational change to PCET and that the altered driving force for F_3Y oxidation, by residues adjacent to it in the pathway, is responsible for this change. Studies with $NH_2Y_{731(730)}$-α2/β2/CDP/ATP resulted in detection of NH_2Y radical (NH_2Y•) intermediates capable of dNDP formation. In this study, the reaction of F_3Y_{356}-β2/α2/CDP/ATP has been examined by stopped flow (SF) absorption and rapid freeze quench EPR spectroscopy and has failed to reveal any radical intermediates. F_3Y_{356}-β2/CDP/ATP has also been examined with NH_2Y_{731}-α2 (or NH_2Y_{730}-α2) by stopped-flow kinetics from pH 6.5–9.2 and revealed rate constants for NH_2Y• formation that support a change in rate limiting step at elevated pH. The results together with kinetic simulations provide a guide for future studies to detect radical intermediates in the pathway.

Ribonucleotide reductases (RNRs) are responsible for reduction of nucleotides to 2′-deoxynucleotides (dNDPs), supplying the precursors required for DNA replication and repair (1,2). Active *E. coli* RNR is a 1:1 complex of two homodimeric subunits: α2 and β2 (3-5). α2 harbors the active site, where thiyl radical-mediated (C_{439}•) nucleotide reduction occurs (6-8), and the binding sites for allosteric effectors, which control the rate and specificity of reduction (9). β2 houses the essential diferric-tyrosyl radical (Y_{122}•) cofactor (10,11). Each turnover requires oxidation of C_{439} in α2 by Y_{122}• in β2 (12). A structure of the active α2β2 complex is unavailable. However, a docking model of this complex, based

[*]To whom correspondence should be addressed. Tel: (617) 253-1814. Fax: (617) 258-7247. stubbe@mit.edu.
[&]Current address: Department of Biological Chemistry and Molecular Pharmacology, 240 Longwood Avenue, C1-609, Boston, MA 02115

Supporting Information Available: SDS-PAGE, UV-vis and EPR characterization of the diferric Y_{122}• cluster in semi-synthetic F_3Y_{356}-β2 after increasing its radical content (Figs. S1 & S2), RFQ EPR traces of additional time points in the reaction of F_3Y_{356}-β2 with wt α2 and CDP/ATP (Fig. S3), stability of NH_2Y_{731}• and NH_2Y_{730}• monitored by UV-vis and EPR spectroscopies (Figs. S4 & S5), magnified views of SF UV-vis traces in the reaction of F_3Y_{356}-β2 with NH_2Y_{731}-α2 or NH_2Y_{730}-α2 (Figs. S6–S8), comparison of the pH profiles of fast k_{obs}s for NH_2Y• formation (Fig. S9). This material is available free of charge via the Internet at http://pubs.acs.org.

on shape complementarity of the structures of the individual subunits, led Uhlin and Eklund to propose that radical transfer between subunits occurs over a distance of 35 Å by a pathway involving aromatic amino acid radicals (Fig. 1 A, B) (13). Mutagenesis studies suggested that the residues shown in Figs. 1A and 1B are important for catalysis (14-16). The inactivity of the mutants, however, precluded mechanistic studies. We have recently incorporated unnatural amino acids site-specifically into the pathway. Our studies have provided direct evidence for the three proposed redox-active tyrosines (Y_{356}, Y_{731} and Y_{730}) (17-19), the pathway dependence (20), and the docking model (21). In the present study, we investigate 2,3,5-F_3Y (F_3Y) site-specifically incorporated in place of Y_{356} in β2 with wt-α2 and with 3-NH_2Y (NH_2Y) incorporated site-specifically in place of Y_{731} or Y_{730} in α2 (Figs. 1A & 1B) using rapid freeze quench (RFQ) EPR and stopped flow (SF) absorption spectroscopies. These studies provide evidence that altering the driving force for oxidation of F_3Y_{356} by adjacent residues in the pathway by raising the pH, can change the rate-limiting step of RNR from a conformational change to proton coupled electron transfer (PCET) and that no radical intermediates are detected.

Y analogs with altered reduction potentials and/or pK_as were of interest for site-specific incorporation into RNR, as oxidation of Y is a PCET process with peak potentials (E_p) being modulated by pH (Fig. 1C) (22-24). Studies on blocked-F_nY analogs, N-acetylated and C-amidated, revealed the appropriateness of these analogs for studying PCET as their phenolic pK_as ranged from 5.6 to 8.4 and their E_ps varied from −50 mV to +270 mV relative to blocked Y in the physiological pH range (25). Perturbation of both of these properties could be mechanistically informative in studying PCET.

Expressed protein ligation (EPL) was used to incorporate F_nYs (where n=1–4) (18,25,26) in place of Y_{356} in β2. To obtain sufficient amounts of semisynthetic β2 to carry out physical biochemical studies, two additional mutations, $V_{353}G$ and $S_{354}C$ in β2, were required. This double mutant, $V_{353}G/S_{354}C$-β2 at pH 7.6 had 25 % the activity of the wt-β2. Henceforth, intein wt-β2 refers to $V_{353}G/S_{354}C$-β2 made by EPL.

The pH rate profiles of F_nY_{356}-β2s with α2, CDP and ATP were studied from pH 6.5 to 9.2 and the ability to produce dNDPs compared to intein wt-β2 (18). Analysis of the rates of dNDP formation relative to intein wt-β2 vs. the relative differences in the E_p of each F_nY relative to Y at each pH (Fig. 1C), revealed three different activity regimes. In the first regime, where the E_p difference between F_nY and Y varied from −40 to +80 mV, the rate-limiting step in dNDP formation is a conformational change that precedes radical transfer. The intein-wt β2 and F_nY-β2s within this range are 100 % active. In the second regime, where the E_p difference increased from +80 to +200 mV greater than Y, the specific activities of mutant RNRs decreased from 100 % to a few %. These data suggested that the rate-limiting step had changed from a conformational change to a step (or steps) in the radical propagation process. Finally, in the third regime, where the E_p difference was greater than 200 mV, no dNDPs are produced and the radical transfer process was completely shut down. If the interpretation of the pH rate profiles of F_nY-β2s is correct, then it may be possible to detect transient intermediates during radical propagation in the second activity regime. Our studies suggested that F_3Y_{356}-β2 would be the most interesting F_nY-β2 to investigate in this regime.

The proposed pathway (Fig. 1A) has been further explored by replacing Y_{730} and Y_{731} in α2 with NH_2Y, a tyrosine analog that is easier to oxidize than Y by 190 mV at pH 7 (Fig. 1C). α in these studies has a single mutation: Y to NH_2Y (27). SF experiments in the presence of β2, CDP and ATP revealed that an NH_2Y radical (NH_2Y•) is generated in a kinetically competent fashion in two phases with rate constants of 18 s^{-1} and 2.5 s^{-1} with $Y_{730}NH_2Y$-α2 and of 12 s^{-1} and 2.5 s^{-1} with $Y_{730}NH_2Y$-α2 at pH 7.6 (19). These studies and more recent

studies (Minnihan, Seyedsayamdost & Stubbe, manuscript in preparation) have further revealed that these mutants can make dNDPs at rates of 0.3–0.6 s^{-1}, substantially slower than the rates of NH_2Y• formation.

In the present paper, F_3Y_{356}-β2 was examined with α2/CDP/ATP to look for radical intermediates by SF and RFQ EPR spectroscopy and none were detected. The hypothesis that an E_p difference of >80 mV between F_3Y and Y changes the rate-determining step of RNR from conformational gating to a step or steps involved in PCET has also been examined: F_3Y-β2 was incubated with NH_2Y_{731}-α2 or NH_2Y_{730}-α2 and the pH rate profile of NH_2Y• formation from pH 6.5 to 9.2 was investigated by SF absorption spectroscopy. The rate constants for NH_2Y• formation are triphasic. Despite the kinetic complexity, they reveal that the pH rate profile for NH_2Y• formation is very similar to that observed previously in the steady state for dNDP formation with F_3Y_{356}-β2/α2/CDP/ATP and are distinct from the steady state data with intein wt-β2 control. A kinetic model to accommodate these results is presented that supports the proposed shift in the rate-limiting step and the kinetic simulations provide an explanation for why transient radical intermediates are not detected. This model provides a framework for future studies involving F_nY incorporation using evolved tRNA/tRNA synthetase pairs, and addressing the importance of W_{48} in the pathway (Figs. 1A & 1B).

Materials and Methods

Materials

[2-^{14}C]-CDP (50 μCi/mL) was purchased from Moravek Biochemicals and calf-intestine alkaline phosphatase (20 U/μL) was from Roche. Lithium 8-hydroxyquinoline-6-sulfonate and Sephadex G-25 were from Sigma. 2-[N-morpholino]-ethanesulfonic acid (Mes), N-2-hydroxethylpiperazine-N′-2-ethanesulfonic acid (Hepes), N-[Tris(hydroxymethyl)methyl] -3-aminopropanesulfonic acid (Taps), 2-[cyclohexylamino]-ethanesulfonic acid (Ches) and Emulsifier-Safe scintillation liquid were obtained from EMD Bioscience. Slide-a-lyzer cassettes were from Pierce. α2 was expressed, purified, and pre-reduced as reported and had a specific activity of 2500 nmol/min mg (18,28). *E. coli* thioredoxin (TR, 40 U/mg) (29) and TR reductase (TRR, 1800 U/mg) were isolated as previously described (30). $Y_{730}NH_2Y$-α2 and $Y_{731}NH_2Y$-α2 were isolated as previously described and had specific activities of 100 and 175 nmol/min mg, respectively (19).

Semisynthesis of F_3Y_{356}-β2

Generation of F_3Y_{356}-β2 by EPL and its purification were carried out as detailed previously (31).

Generation of apo F_3Y_{356}-β2 with lithium 8-hydroxyquinoline-6-sulfonate

The apo form of intein wt-β2 and F_3Y_{356}-β2 were generated by a modification of the procedure of Atkin et al (32). Briefly, a solution of 2.5 mL of each β2 variant (~20 mg, 90 μM) was dialyzed against 500 mL of chelator solution consisting of 1 M imidazole, 30 mM NH_2OH, 50 mM 8-hydroxyquinoline-6-sulfonate (pH 7.0) in a 3 mL Slide-a-lyzer cassette for 3 h. The chelator was then removed by dialysis against 4 L Hepes buffer (50 mM Hepes, 5 % glycerol, pH 7.6) for 3 h and further by desalting on a Sephadex G 25 column (1.5 × 23, 40 mL) equilibrated in Hepes buffer. This procedure gives the apo form of each β2 variant in 80–95 % yield. The concentration of apo β2 was determined using $\varepsilon_{280\ nm}$ = 120 $mM^{-1}cm^{-1}$.

Reconstitution of apo β2

The apo form of each β2 variant was reconstituted as reported previously. This procedure yields a radical content of ~1.2 Y_{122}•/β2 as determined by the dropline procedure (33).

Spectrophotometric and radioactive RNR Assays

RNR activity assays were performed as previously described (18). The final concentration of α2 and β2 variants in these assays were each 3 μM. The specific activity of [2-^{14}C] -CDP was 3800 cpm/nmol.

Single Wavelength and Diode Array SF Absorption Spectroscopy

SF absorption kinetics were performed on an Applied Photophysics DX. 17MV instrument equipped with the Pro-Data upgrade. The temperature was maintained at 25°C with a Lauda RE106 circulating water bath. Single wavelength kinetics experiments utilized PMT detection at 410 nm (λ_{max} of Y_{122}• with $\varepsilon = 3700\ M^{-1}cm^{-1}$) (33), 510 nm ($\lambda_{max}$ of W• with $\varepsilon = 2200\ M^{-1}cm^{-1}$) and 560 nm ($\lambda_{max}$ of $WH^{\bullet+}$ with $\varepsilon = 3000\ M^{-1}cm^{-1}$) (34). Typically, pre-reduced α2 (50–70 μM) and ATP (6 mM) in one syringe were mixed with F_3Y_{356}-β2 (50–70 μM) and CDP (2 mM) in a 1:1 ratio in 50 mM Taps, 15 mM $MgSO_4$, 1 mM EDTA, pH 8.4. Time courses shown are the average of at least 5 individual traces. Diode array SF absorption spectroscopy was carried out with an Applied Photophysics PDA.1 Photodiode Array detector. The concentration of the reaction components were the same as described for single wavelength kinetics.

RFQ EPR Spectroscopy

RFQ EPR samples were prepared using an Update Instruments 1019 Syringe Ram Unit, a Model 715 Syringe Ram Controller and a quenching bath. The temperature of the liquid isopentane bath was controlled with a Fluke 52 Dual Input Thermometer, equipped with an Anritsu Cu Thermocouple probe for the isopentane bath and the funnel. Stainless steel packers were purchased from McMaster-Carr and were cut to a length of 40 cm and deburred at the MIT machine shop. The dead-time of the set-up was determined to be 16 ± 2 ms with two independent measurements of the myoglobin/NaN_3 test reaction. A packing factor of 0.60 ± 0.05 was reproducibly obtained as tested with intein-wt β2 samples. Routinely, a ram push velocity of 1.25 or 1.6 cm/s was used and the displacement was adjusted to expel 300 μL sample after the reaction.

Operation of the apparatus was similar to the procedure previously described (35). Typically, pre-reduced α2 (50–70 μM) and ATP (6 mM) in one syringe were mixed with F_3Y_{356}-β2 and CDP (2 mM) in the second syringe in a 1:1 ratio in 50 mM Taps, 15 mM $MgSO_4$, 1 mM EDTA, pH 8.4. When the temperature of the EPR tube-funnel assembly had equilibrated to the bath temperature, the contents of each syringe were mixed rapidly in a mixing chamber and aged for a pre-determined time period by pushing the contents through a reaction loop. The sample was sprayed into the EPR tube-funnel assembly which was held at a distance of ≤1 cm from the spray nozzle. The assembly was immediately returned to the bath and the crystals allowed to settle for 15–30 s. The sample was then packed into the EPR tube using the stainless steel packers described above.

EPR spectra were recorded at the Department of Chemistry Instrumentation Facility on a Bruker ESP-300 X-band (9.4 GHz) spectrometer. Spectra at 77 K were recorded with a quartz finger dewar filled with liquid N_2; spectra at 15 K were acquired with an Oxford liquid helium cryostat and an Oxford ITC 503 temperature controller. Unless noted otherwise, EPR parameters were as follows: Power = 50 μW, modulation amplitude = 1.5 G, modulation frequency = 100 kHz, time constant = 5.12 ms and scan time = 41.9 s.

pH Rate Profile of NH_2Y• Formation in the Reaction of F_3Y_{356}-β2 with NH_2Y-α2s monitored by SF-Absorption Spectroscopy

NH_2Y-α2 was prepared and pre-reduced as detailed previously (19). In all experiments, pre-reduced NH_2Y-α2 and ATP were mixed with F_3Y_{356}-β2 and CDP to yield final concentrations of 4 μM, 3 mM, 4 μM and 1 mM, respectively. Single wavelength kinetics were monitored using PMT detection at 320 nm (λ_{max} of NH_2Y_{731}• with ε = 11000 $M^{-1}cm^{-1}$) or 325 nm (λ_{max} of NH_2Y_{730}• with ε = 10500 $M^{-1}cm^{-1}$) (19). Reactions were carried out in 15 mM $MgSO_4$, 1 mM EDTA and 50 mM Goods Buffers [Mes (pH 6.5–7), Hepes (pH 7–8), Taps (pH 8–8.8) or Ches (pH 8.8–9.2) buffer] adjusted to the desired pH. Syringes and reaction lines were equilibrated in the desired buffer prior to the experiment. At each pH, 6-8 traces were averaged and analyzed using OriginPro Software. Iterative rounds of fitting were carried out until the R^2 value was maximized (≥0.99) and the residual plot was randomly scattered around zero ± ≤0.001 AU.

Results

Pre-steady State Experimental Design

Previous pre-steady state examination of wt RNR at pH 7.6 has shown that production of dCDP is rate-limited by a conformational change that precedes radical transfer, resulting in a burst of dCDP formation in the first turnover with rate constants of 4.4–10 s^{-1} (36). In wt RNR, this conformational change(s) kinetically masks detection of the proposed aromatic amino acid radical intermediates during radical transfer (Figs. 1A & 1B). Thus, detection of transient radical intermediates requires, at a minimum, that the rate constant for radical transfer be diminished relative to that for the conformational step. Our previous results with F_nY-β2s suggested that insertion of F_3Y in place of Y_{356} provides a sufficient shift in the driving force for radical propagation, to make it rate-limiting at elevated pH (18). Thus it is possible that pathway radical intermediates could be detected by RFQ EPR methods at elevated pH.

Increasing the Y_{122}• Radical Content of Semisynthetic F_3Y_{356}-β2

To maximize our chances of detecting low levels of pathway radical intermediates, we focused on increasing the concentration of Y_{122}• in the semisynthetic β2s using the method of Atkins et al. (32). With both intein wt-β2 and F_3Y_{356}-β2, we were able to obtain ~1.2 Y_{122}•/β2 with good protein recoveries (80 to 95 %). The UV-vis spectrum, EPR spectrum, and SDS PAGE of these proteins are shown in Figs. S1 and S2. The spectra are identical to those of recombinant wt-β2 indicating an intact diferric-Y_{122}• cofactor. Assays for dCDP production before and after application of this procedure, gave specific activities that correlated with Y_{122}• content. Thus, the procedure increased the radical content of F_3Y-β2 and elevated nucleotide reduction activity proportionally.

SF Absorption and RFQ EPR Spectroscopies with F_3Y_{356}-β2/α2

To test whether radical intermediates could be detected during the radical propagation process with F_3Y_{356}-β2 at pH 8.4, where this process is proposed to be rate-limiting, SF absorption and RFQ EPR studies were carried out with wt α2. Using the E_ps measured for the blocked amino acids, W, F_3Y, Y and NH_2Y (Fig. 1C), an energy landscape for the pathway (Fig. 1D) was created to help visualize how insertion of F_3Y into the pathway and pH might alter the ability of adjacent residues in the pathway to mediate its oxidation. If forward radical transfer is slow at pH 8.4 for example, then a neutral W_{48} could build up, if it is not rapidly reduced by Y_{122}. W•s have reported λ_{max}s from 485–530 nm (ε = 1750–2300 $M^{-1}cm^{-1}$). We also considered the possibility that WH•+ might be observed and they have reported λ_{max}s between 560–600 (ε = 2500–2900 $M^{-1}cm^{-1}$) (34,37). If reverse radical

transfer is slow, then the species most likely to build up at pH 8.4 is the Y_{731}•, based on E_p difference of 110 mV relative to F_3Y (Figs. 1C & 1D). Y•s have λ_{max}s in the range of 407–410 (ε = 2750–3200 $M^{-1}cm^{-1}$) (38,39). The results from SF absorption experiments are presented in Fig. 2A. They show that no changes are observed at 410 nm (λ_{max} for Y_{122}•), 510 nm or 560 nm. The minor changes that are observed are likely related to small structural perturbations associated with the di-iron cluster upon binding to α2 (20). SF diode array absorption spectroscopy also failed to reveal any changes in the region of 400-800 nm (data not shown). Under these experimental conditions, no absorption features associated with a W• or WH•+ were apparent.

As mentioned above, the absorption features associated with the Y• range from 407–410 nm with varying degrees of sharpness. The Y_{122}• and Y_{731}• features are thus likely to be similar, making build up of a transient Y_{731}• difficult to distinguish from Y_{122}• by vis spectroscopy. The EPR features of Y_{122}• and Y_{731}•, on the other hand, are highly dependent on the dihedral angle of the β protons relative to the aromatic ring (40,41). Based on the crystal structures of α2 and β2, Y_{122}, Y_{731} and Y_{730} have dihedral angles of ~90°, 33° and 37°, respectively (13), making it feasible that the EPR spectra of the latter two would be distinct from that of Y_{122}• (42). In accord with the structural data, we recently determined a dihedral angle of 46° for NH_2Y_{730}• by EPR analysis (43). Consequently, RFQ-EPR studies were carried out under conditions similar to those in the SF absorption experiments to look for a new Y•. The reaction was quenched from 28 to 1912 ms. The traces obtained at 72, 138 and 1912 ms are shown in Fig. 2B and those at 28 and 612 ms in Fig. S3. EPR analysis and spin quantitation at 77 K or 15 K at all time points showed that the [Y•] observed is identical to the [Y_{122}•] at time zero. The SF absorption and RFQ EPR spectroscopy experiments have thus failed to reveal formation of any pathway radical intermediates. We estimate that the lower limit of detection of W•s by SF spectroscopy would be 1 μM, ~3 % of the amount of protein. The lower limit for Y• detection by EPR methods is 1.5–3 μM and is estimated to be 5–10 % of the protein. A rationalization for the lack of build-up of intermediates is presented below.

Use of NH_2Y-α2 as a Reporter of Forward Radical Transfer with F_3Y_{356}-β2

Our previous SF studies at pH 7.6 with β2, $Y_{731}NH_2Y$-α2 (or $Y_{730}NH_2Y$-α2), CDP/ATP revealed that NH_2Y• is formed with biphasic kinetics and rate constants of 18 s^{-1} and 2.5 s^{-1} (12 s^{-1} and 2.5 s^{-1}) (19). The faster rate constants were proposed to be associated with electron delocalization within the protein in a non-productive conformation for nucleotide reduction, with NH_2Y• formation resulting due to the ease of its oxidation. The slower rate constants were proposed to be associated with the rate limiting conformational change responsible for dNDP production under steady state conditions. NH_2Y• formation was “complete” within 20 s and its concentration remained unchanged for several minutes. The decay of NH_2Y• is slow with a rate constant of 0.0062 ± 0.0012 for NH_2Y_{731}• (Fig. S4) and 0.0043 ± 0.0011 s^{-1} for NH_2Y_{730}• (Fig. S5). Finally both 730 and 731 NH_2Y mutants supported dCDP formation with rate constants of 0.3–0.6 s^{-1}, substantially lower than the rate constant of NH_2Y• production (Minnihan, Seyedsayamdost & Stubbe, manuscript in preparation). These rate constants would be further reduced with F_3Y_{356}-β2, as intein wt-β2 has 25 % the activity of wt-β2. These observations together suggest that under the conditions of the SF experiments described subsequently, NH_2Y can function as a radical trap reporting on the rate constant for forward radical propagation.

SF Absorption Spectroscopy with F_3Y_{356}-β2/NH_2Y-α2/CDP/ATP

SF experiments were thus carried out with F_3Y_{356}-β2 and NH_2Y_{730}-α2 or NH_2Y_{731}-α2. The final concentration of protein in these experiments was 4 μM, similar to those previously

reported in the steady state pH rate profile studies (3 μM) (36). The ability to generate 1.2 Y_{122}• per $Y_{356}F_3Y$-β2, greatly facilitated the analysis.

The results of the pH-dependent SF experiments with NH_2Y_{730}-α2 (or NH_2Y_{731}-α2) and F_3Y_{356}-β2 are shown in Fig. 3. Expanded views of the first several seconds of each trace are shown in Fig. S6 (for $Y_{731}NH_2Y$-α2) and Fig. S7 (for $Y_{730}NH_2Y$-α2). Reactions monitored for 20 s at pH 6.5, 8.45 and 8.6 (for $Y_{731}NH_2Y$-α2) and at 8.65 (for $Y_{730}NH_2Y$-α2) are shown in Fig. S8. The kinetic parameters are summarized in Table 1.

Fits to the kinetic traces in all cases required three exponentials. These results contrast to those with wt-β2/NH_2Y-α2, which generate a NH_2Y• with all substrate/effector pairs in two kinetic phases. The molecular basis for the different phases is not understood, but our interpretation is that the slowest kinetic phase is associated with dCDP formation as observed in the steady state pH rate profile studies with F_3Y_{356}-β2/α2 and CDP/ATP (18). The second, kinetic phase may be associated with the mutations ($V_{353}G$ and $S_{354}C$) that, as noted above, are required for efficient semisynthesis of β2. We propose that these two residues are likely located at the α2/β2 interface generating an additional conformation that binds to α2 and results in NH_2Y• formation. We propose that the fastest phase is associated with non-productive conformational changes, as noted above. Three kinetic phases have previously been observed when fitting the data associated with 3-hydroxytyrosine radical (DOPA•) formation from DOPA-β2/α2/CDP/ATP, also made by the EPL method (17). The analysis of these pH profiles presented below focuses mainly on the slowest, third kinetic phase, as it corresponds to dCDP production in the steady state.

Analysis of the pH rate profile for NH_2Y• formation with F_3Y_{356}-β2/NH_2Y-α2

The pH dependence of wt RNR activity is not understood, but is associated with conformational changes and not chemistry. In the current case, pH is used to modulate the driving force for radical transfer (Figs. 1C & 1D) based on our previously observed correlation between the rate of dNDP formation and the E_p difference between F_3Y and Y between pH 7.8 and 8.7. To analyze the results in Fig. 3, the rate constants for NH_2Y• formation were plotted as a function of pH for each kinetic phase (Figs. 4A–4C).

The data from the fastest phase with NH_2Y_{730}-α2 (Fig. 4A, blue dots) and NH_2Y_{731}-α2 (Fig. 4A, red dots) exhibited k_{obs}s that vary from 2.7–48.9 s^{-1} and from 7.8–26.2 s^{-1}, respectively. The amplitudes in this phase account for the smallest amount, 10–26 %, of the total NH_2Y•. Furthermore, unlike the other phases, the profile for NH_2Y_{731}-α2 is distinct from NH_2Y_{730}-α2 (Figs. 4A and S9). The second kinetic phase exhibits rate constants from 0.38–3.8 s^{-1} (0.80–3.0 s^{-1}) with amplitudes of 37–50 % of the total absorbance change (Fig. 4B, blue dots and red dots), while the k_{obs}s for the third kinetic phase vary from 0.11–0.52 s^{-1} (0.09–0.42 s^{-1}) with amplitudes of 27–52 % of the overall change (Fig. 4C, blue dots and red dots). The profiles of the two slow kinetic phases have shapes very similar to that observed for dCDP formation with F_3Y-β2.

Our hypothesis is that the slowest kinetic phase is associated with the RNR conformation active in turnover. To analyze this phase further, the rate constants for NH_2Y• formation with both 730 and 731 mutants were overlaid with those for dCDP formation in the steady state (Fig. 4D). Also included is the profile for dCDP formation with intein wt-β2 (green squares). A direct comparison between the rate constants for pre-steady state NH_2Y• formation and steady state dCDP formation (by F_3Y_{356}-β2/α2) as a function of pH shows remarkable agreement. They overlap in all three activity regimes and are distinct from that of intein wt-β2 at pH > 7.8 (Fig. 4D, green squares). Because NH_2Y• formation serves as a read-out for forward radical transfer, the results indicate that a step in this process has the same pH-dependent rate constants as k_{cat} measured by steady state kinetic assays. This

observation supports our original proposal that at high pH, the rate-determining step has shifted from a physical step to radical transfer and suggests that insertion of F_3Y results in a decrease in the rate constant for forward radical transfer as the reaction pH is increased.

Discussion

Kinetic Simulations

To address our inability to detect radical intermediates with F_3Y_{356}-β2, despite an apparent shift in the rate-determining step, kinetic simulation studies have been carried out. Fig. 1D will be used as a means to predict the potential build-up of intermediates associated with F_3Y insertion into the pathway. This energy landscape model of the pathway assumes that the reduction potentials and pK_as of the residues involved are minimally perturbed by the protein environment. For residues Y_{356} in β2 and Y_{730} and Y_{731} in α2, these assumptions are supported by our recent studies in which 3-nitrotyrosine (NO_2Y) has been site specifically incorporated into each of these positions (44,45). The model suggests that during forward PCET, the step most likely to be rate-limiting at pH 8.4 would be the oxidation of F_3Y by the W_{48}• based on E_ps of 0.85 V and 0.8 V, respectively, (Figs. 1C & 1D). In the reverse direction at pH 8.4, the slowest step would be the oxidation of F_3Y by Y_{731}• consistent with E_ps of 0.85 V and 0.74 V, respectively (Figs. 1C & 1D).

The kinetic model in Fig. 5 is based on our previous kinetic model for wt RNR at pH 7.6 and the data and simulations reported herein (Fig. 5) (36). Two points should be reiterated prior to presentation of the model in detail. The first is that intein-wt β2 has 25 % the activity of wt-β2 due to the two additional mutations. Thus, the rate constants associated with the conformational change(s) used in the model could be elevated 4-fold for the wt RNR. The second is that while W_{48} has been incorporated into the original pathway model (13) and all subsequent renditions of this model (15,24,46), there is currently no direct evidence for its involvement in contrast with the proposed Y pathway residues. While in our model we have incorporated this residue, we and others are actively trying to address its involvement using multiple methods (45,46).

In the model in Fig. 5, binding of CDP and effector ATP, step A, is followed by the rate-limiting conformational change, step B, that gates radical transfer. Subsequent to this change, Y_{122}• is reduced and gives rise to a W_{48}•, step C, which then generates a C_{439}• via F_3Y_{356}, Y_{731} and Y_{730} transient radical intermediates, step D. One hopping step within step D, oxidation of F_3Y by W_{48}•, is proposed to be the rate-limiting step in the forward direction. C_{439}• catalyzes nucleotide reduction, step E, which then gives rise to Y_{731}• through a transient Y_{730}• intermediate, step F. Y_{731}• then regenerates Y_{122}• via F_3Y_{356} and W_{48}, step G; this step could represent the rate-limiting step in reverse radical transfer. Dissociation of dCDP, step H, completes the catalytic cycle, although in the steady state the active site disulfide needs to be re-reduced for multiple turnovers to occur. In this model, the K_ds and rate constants in black (steps A, E, F and H) have been determined experimentally (45,47,48). A rate constant of 107 s^{-1} for dCDP formation, step E, and 100 s^{-1} for Y_{356}• formation, step F, have been recently determined in studies using NO_2Y site-specifically incorporated in place of Y_{122} (NO_2Y_{122}-β2) (45). This protein does not have the additional mutations of the EPL-generated protein. A NO_2Y• is transiently generated at position 122, that uncouples proton and electron transfer and unmasks for the first time, the rate constant of dCDP formation and for Y_{356}• formation in the reverse direction. The rate constants in grey (steps C, F and k_{rev} in step B) were used in our original kinetic model for wt-RNR (pH 7.6) to reproduce our inability to observe disappearance and reappearance of Y_{122}• or to detect any radical intermediates under a wide range of conditions (36). The rate constants in red (k_{fwd} in steps B, D, and G) have been determined experimentally herein and assigned to these steps as described subsequently. Note that the rate constant associated with step B (0.5

s^{-1}) might be elevated 4-fold as described above. The rate constants in blue have been simulated herein.

We began this exercise by simulating the effect of a solely rate-limiting reverse radical transfer. In this case, step D and the intermediate preceding it were eliminated from the model, and we assigned to step G the k_{obs} of 0.2 s^{-1}, obtained at pH 8.4 by SF absorption spectroscopy for NH_2Y• formation (see Table 1). This assignment is consistent with E_p differences between F_3Y and Y at pH 8.4 described above (25). The simulations show that with 20 μM RNR, Y_{731}• would build up to > 12.5–14 μM. The RFQ-EPR studies, however, failed to detect any new Y•. Changing the parameters for step C (100–300 s^{-1} for k_{rev}) or step G (1-100 s^{-1} for k_{rev}) still yielded >12 μM of Y_{731}•. Thus, within the current kinetic framework, and the caveat that the Y• would have detectable hyperfine by EPR spectroscopy (42), reverse radical transfer is not solely rate-limiting, consistent with our SF absorption studies where NH_2Y-α2 served as a reporter for forward radical transfer.

We next assumed a solely rate-limiting forward radical transfer. In this case, step G and the intermediate preceding it were eliminated from the model (Fig. 5) and the slow step of 0.2 s^{-1} at pH 8.4 (see Table 1) was applied to step D, consistent with E_p difference between W and F_3Y (Figs. 1C & 1D). The kinetic simulations show at 20 μM RNR, that W_{48}• accumulates to 0.5–1.4 μM (using 10^2–10^3 s^{-1} for step F and 300 s^{-1} for k_{rev} of step C). As discussed above, these concentrations are at or below our lower limit of detection. In addition, given the half-sites reactivity for RNRs that we have observed in many of our experiments (17,19), the actual concentration of the radical would be even lower (0.25–0.7 μM). The k_{rev} for step C had to be increased to ≥ 300 s^{-1} relative to our original kinetic model for RNR (200 s^{-1}) in order to reproduce our inability to detect intermediates. This suggests an increased flux toward Y_{122}• reformation when F_3Y_{356} replaces Y_{356}• The faster the k_{rev} for steps B or C, the lower the amount of W_{48}• that would build up. This simulation makes it much less likely that a $W_{48}H$•+ is involved during forward PCET (Figs. 1C & 1D, see below).

Finally, we assumed that forward *and* reverse radical transfers are both partially rate-limiting and assign steps D and G both to 0.2 s^{-1}. In this case, the simulations show that Y_{731}• and W_{48}• would build up to <0.8 μM and 0.25–0.7 μM (after accounting for half-sites reactivity), respectively. Thus, within the framework of the current model, rate-limiting forward or partially rate-limiting forward *and* reverse PCET are consistent with the inability to observe intermediates despite an apparent change in rate-limiting radical transfer as a result of F_3Y insertion into the pathway. This model serves as a starting point for examining the kinetics of F_3Y_{356}-β2 further, for example by using rapid chemical quench methodology to examine the rate of dCDP formation. The two models make different predictions about the lag phases in dCDP production. Evolution of a tRNA/tRNA synthetase pair for incorporation of F_3Y is in progress. These studies should remove the kinetic complexity associated with the two additional mutations required by EPL method, increase the overall activity 4 fold and make further analysis simpler.

Implications for Radical Propagation

Despite the shift in the rate-determining step associated with the redox properties of F_3Y relative to W_{48} or Y_{731} (Figs. 1C & 1D), no pathway intermediates are detectable. A modeling exercise incorporating recent kinetic parameters from studies with Y_{122} replaced with NO_2Y, provides insight as to why this might be the case, and if W_{48} is on the pathway, as to why a W• and not a WH•+ is the most likely intermediate between Y_{122} and residue 356. We consider the WH•+ less likely given the following argument. If we assume the pK_a of F_3Y is minimally perturbed (44) and that a WH•+ participates in the pathway, the E_p difference between WH•+ and F_3Y would not change between pH 7 and 8.4 (Fig. 1C). Our

data indicates that the rate-determining step occurs between Y_{122}• reduction and NH_2Y oxidation. Therefore, the rate-limiting step would be associated with oxidation of W_{48} by Y_{122}• (oxidation of F_3Y by WH•+ is pH-independent and that of Y_{731} by F_3Y• is thermodynamically favored, Fig. 1D). This conclusion is inconsistent with the observation that when F_nYs are placed in position 356, their pH rate profiles differ from intein wt-β2. They would be the same if Y_{122}•-mediated W oxidation was slow. It is also inconsistent with the >200 mV E_p difference (Fig. 1D, Y_{122} is special and appears to be a thermodynamic hole) at pH 7 and a >310 mV difference at pH 8.4 between Y_{122} and WH•+. With W_{48}• as an intermediate, on the other hand, an explanation for the change in rate-determining step when F_3Y is inserted into the pathway becomes apparent. In the case of the neutral W•, the E_p gap between Y_{122} and W_{48} does not change as a function of pH, F_3Y•-mediated oxidation of Y or NH_2Y is thermodynamically very favorable (Fig. 1D), and thus oxidation of F_3Y by W_{48}• remains as the basis for the observed changes. Between pH 7 and 8.4 (Fig. 1C) the reaction becomes less favorable by 70 mV.

While our previous studies have demonstrated the importance of a WH•+ in active metallo-cofactor assemble and more specifically Y_{122} oxidation (49,50), in this case the reaction is irreversible, in contrast to the reversible PCET pathway (Fig. 1), and the "hot" Fe^{4+}/Fe^{3+} oxidant could drive the reaction toward the Y•. These studies and our other studies suggest that Nature has chosen W and Y as reversible redox conduits over long distances as their reduction potentials require minimal perturbation. W and Y contrast to many metal or organic cofactors (flavins, hemes) used by enzymes in which the protein environment must modulate the reduction potentials by >500 mV for the cofactor to function (51,52). W and Y have the appropriate chemical properties for fine-tuning the unusual radical propagation pathway in RNR.

The kinetic modeling provides a framework to think about optimal unnatural amino acids to perturb the pathway to detect intermediates and to study the PCET process at each step. For example, the model suggests that to detect intermediates in the pathway, a hot oxidant needs to replace the Y_{122}•. Rapid reduction of the hot oxidant would lead to rapid production of pathway intermediates that would be unable to reoxidize the reduced form of the oxidant, allowing build up an intermediate(s). This approach has recently been shown to be successful by placing NO_2Y at position 122 that can be oxidized by the Fe^{4+}/Fe^{3+} radical, but cannot be reoxidized by pathway radicals (45). The studies further suggest that NH_2Y substitution will be useful in examining the individual hopping steps of the three transiently involved Y•s in the pathway.

Supplementary Material

Refer to Web version on PubMed Central for supplementary material.

Acknowledgments

We would like to thank Ellen C. Minnhan for helpful discussions and the NIH (Grant 29595 to J.S.) for support of this work. M.R.S. is a Novartis Fellow of the Life Sciences Research Foundation.

References

1. Stubbe J, van der Donk WA. Protein radicals in enzyme catalysis. Chem Rev. 1998; 98:705–762. [PubMed: 11848913]
2. Jordan A, Reichard P. Ribonucleotide reductases. Annu Rev Biochem. 1998; 67:71–98. [PubMed: 9759483]
3. Brown NC, Reichard P. Ribonucleoside diphosphate reductase. Formation of active and inactive complexes of proteins B1 and B2. J Mol Biol. 1969; 46:25–38. [PubMed: 4902211]

4. Thelander L. Physicochemical characterization of ribonucleoside diphosphate reductase from *Escherichia coli*. J Biol Chem. 1973; 248:4591–4601. [PubMed: 4578086]
5. Wang J, Lohman GJ, Stubbe J. Enhanced subunit interactions with gemcitabine-5′-diphosphate inhibit ribonucleotide reductases. Proc Natl Acad Sci U S A. 2007; 104:14324–14329. [PubMed: 17726094]
6. Stubbe J. Ribonucleotide reductases: amazing and confusing. J Biol Chem. 1990; 265:5329–5332. [PubMed: 2180924]
7. Stubbe J. Ribonucleotide reductases in the twenty-first century. Proc Natl Acad Sci U S A. 1998; 95:2723–2724. [PubMed: 9501154]
8. Licht S, Gerfen GG, Stubbe J. Thiyl radicals in ribonucleotide reductases. Science. 1996; 271:477–481. [PubMed: 8560260]
9. Nordlund P, Reichard P. Ribonucleotide reductases. Annu Rev Biochem. 2006; 75:681–706. [PubMed: 16756507]
10. Ehrenberg A, Reichard P. Electron spin resonance of the iron-containing protein B2 from ribonucleotide reductase. J Biol Chem. 1972; 247:3485–3488. [PubMed: 4337857]
11. Sjöberg BM, Reichard P, Gräslund A, Ehrenberg A. The tyrosine free radical in ribonucleotide reductase from *Escherichia coli*. J Biol Chem. 1978; 253:6863–6865. [PubMed: 211133]
12. Stubbe J, Nocera DG, Yee CS, Chang MCY. Radical initiation in the class I ribonucleotide reductase: long-range proton-coupled electron transfer? Chem Rev. 2003; 103:2167–2201. [PubMed: 12797828]
13. Uhlin U, Eklund H. Structure of ribonucleotide reductase protein R1. Nature. 1994; 370:533–539. [PubMed: 8052308]
14. Climent I, Sjöberg BM, Huang CY. Site-directed mutagenesis and deletion of the carboxyl terminus of *Escherichia coli* ribonucleotide reductase protein R2. Effects on catalytic activity and subunit interaction. Biochemistry. 1992; 31:4801–4807. [PubMed: 1591241]
15. Ekberg M, Sahlin M, Eriksson M, Sjöberg BM. Two conserved tyrosine residues in protein R1 participate in an intermolecular electron transfer in ribonucleotide reductase. J Biol Chem. 1996; 271:20655–20659. [PubMed: 8702814]
16. Ekberg M, Birgander P, Sjöberg BM. In vivo assay for low-activity mutant forms of *Escherichia coli* ribonucleotide reductase. J Bacteriol. 2003; 185:1167–1173. [PubMed: 12562785]
17. Seyedsayamdost MR, Stubbe J. Site-specific replacement of Y_{356} with 3,4-dihydroxyphenylalanine in the β_2 subunit of *E. coli* ribonucleotide reductase. J Am Chem Soc. 2006; 128:2522–2523. [PubMed: 16492021]
18. Seyedsayamdost MR, Yee CS, Reece SY, Nocera DG, Stubbe J. pH rate profiles of F_nY_{356}-R2s (n = 2, 3, 4) in *Escherichia coli* ribonucleotide reductase: evidence that Y_{356} is a redox-active amino acid along the radical propagation pathway. J Am Chem Soc. 2006; 128:1562–1568. [PubMed: 16448127]
19. Seyedsayamdost MR, Xie J, Chan CT, Schultz PG, Stubbe J. Replacement of Y730 and Y731 in the alpha2 subunit of *Escherichia coli* ribonucleotide reductase with 3-aminotyrosine using an evolved suppressor tRNA/tRNA-synthetase pair. J Am Chem Soc. 2007; 129:15060–15071. [PubMed: 17990884]
20. Minnihan EC, Seyedsayamdost MR, Stubbe J. Use of 3-aminotyrosine to examine the pathway dependence of radical propagation in *Escherichia coli* ribonucleotide reductase. Biochemistry. 2009; 48:12125–12132. [PubMed: 19916558]
21. Seyedsayamdost MR, Chan CT, Mugnaini V, Stubbe J, Bennati M. PELDOR spectroscopy with DOPA-β2 and NH_2Y-α2s: distance measurements between residues involved in the radical propagation pathway of *E. coli* ribonucleotide reductase. J Am Chem Soc. 2007; 129:15748–15749. [PubMed: 18047343]
22. Tommos C, Skalicky JJ, Pilloud DL, Wand AJ, Dutton PL. *De novo* proteins as models of radical enzymes. Biochemistry. 1999; 38:9495–9507. [PubMed: 10413527]
23. Reece SY, Stubbe J, Nocera DG. pH Dependence of charge transfer between tryptophan and tyrosine in dipeptides. Biochim Biophys Acta. 2005; 1706:232–238. [PubMed: 15694351]

24. Reece SY, Hodgkiss JM, Stubbe J, Nocera DG. Proton-coupled electron transfer: the mechanistic underpinning for radical transport and catalysis in biology. Philos Trans R Soc London, Ser B. 2006; 361:1351–1364. [PubMed: 16873123]
25. Seyedsayamdost MR, Reece SY, Nocera DG, Stubbe J. Mono-, di-, tri-, and tetra-substituted fluorotyrosines: new probes for enzymes that use tyrosyl radicals in catalysis. J Am Chem Soc. 2006; 128:1569–1579. [PubMed: 16448128]
26. Reece SY, Seyedsayamdost MR, Stubbe J, Nocera DG. Electron transfer reactions of fluorotyrosyl radicals. J Am Chem Soc. 2006; 128:13654–13655. [PubMed: 17044670]
27. DeFelippis MR, Murthy CP, Broitman F, Weinraub D, Faraggi M, Klapper MH. Electrochemical properties of tyrosine phenoxy and tryptophan indolyl radicals in peptides and amino acid analogs. J Phys Chem. 1991; 95:3416–3419.
28. Salowe S, Bollinger JM Jr, Ator M, Stubbe J. Alternative model for mechanism-based inhibition of *Escherichia coli* ribonucleotide reductase by 2′-azido-2′-deoxyuridine 5′-diphosphate. Biochemistry. 1993; 32:12749–12760. [PubMed: 8251496]
29. Chivers PT, Prehoda KE, Volkman BF, Kim BM, Markley JL, Raines RT. Microscopic p*K*a values of *Escherichia coli* thioredoxin. Biochemistry. 1997; 36:14985–14991. [PubMed: 9398223]
30. Russel M, Model P. Direct cloning of the trxB gene that encodes thioredoxin reductase. J Bacteriol. 1985; 163:238–242. [PubMed: 2989245]
31. Yee CS, Seyedsayamdost MR, Chang MCY, Nocera DG, Stubbe J. Generation of the R2 subunit of ribonucleotide reductase by intein chemistry: insertion of 3-nitrotyrosine at residue 356 as a probe of the radical initiation process. Biochemistry. 2003; 42:14541–14552. [PubMed: 14661967]
32. Atkin CL, Thelander L, Reichard P, Lang G. Iron and free radical in ribonucleotide reductase. Exchange of iron and Mossbauer spectroscopy of the protein B2 subunit of the *Escherichia coli* enzyme. J Biol Chem. 1973; 248:7464–7472. [PubMed: 4355582]
33. Bollinger JM Jr, Tong WH, Ravi N, Huynh BH, Edmondson DE, Stubbe J. Use of rapid kinetics methods to study the assembly of the diferric-tyrosyl radical cofactor of *E. coli* ribonucleotide reductase. Methods Enzymol. 1995; 258:278–303. [PubMed: 8524156]
34. Aubert C, Vos MH, Mathis P, Eker AP, Brettel K. Intraprotein radical transfer during photoactivation of DNA photolyase. Nature. 2000; 405:586–590. [PubMed: 10850720]
35. Ballou DP. Freeze-quench and chemical-quench techniques. Methods Enzymol. 1978; 54:85–93. [PubMed: 215881]
36. Ge J, Yu G, Ator MA, Stubbe J. Pre-steady-state and steady-state kinetic analysis of *E. coli* class I ribonucleotide reductase. Biochemistry. 2003; 42:10071–10083. [PubMed: 12939135]
37. Baugher JF, Grossweiner LI. Photolysis mechanism of aqueous tryptophan. J Phys Chem. 1977; 81:1349–1354.
38. Feitelson J, Hayon E. Electron ejection and electron capture by phenolic compounds. J Phys Chem. 1973; 77:10–15.
39. Bansal KM, Fessenden RW. Pulse radiolysis studies of the oxidation of phenols by $\bullet SO_4^-$ and Br_2^- in aqueous solutions. Radiat Res. 1976; 67:1–8. [PubMed: 940923]
40. Pesavento RP, van der Donk WA. Tyrosyl radical cofactors. Adv Prot Chem. 2001; 58:317–385.
41. Lendzian F. Structure and interactions of amino acid radicals in class I ribonucleotide reductase studied by ENDOR and high-field EPR spectroscopy. Biochim Biophys Acta. 2005; 1707:67–90. [PubMed: 15721607]
42. Svistunenko DA, Cooper CE. A new method of identifying the site of tyrosyl radicals in proteins. Biochem J. 2004; 87:582–595.
43. Seyedsayamdost MR, Argirevic T, Minnihan EC, Stubbe J, Bennati M. Structural examination of the transient 3-aminotyrosyl radical on the PCET pathway of *E. coli* ribonucleotide reductase by multifrequency EPR spectroscopy. J Am Chem Soc. 2009; 131:15729–15738. [PubMed: 19821570]
44. Yokoyama K, Uhlin U, Stubbe J. Site-specific incorporation of 3-nitrotyrosine as a probe of pKa perturbation of redox-active tyrosines in ribonucleotide reductase. J Am Chem Soc. 2010; 132:8385–8397. [PubMed: 20518462]

45. Yokoyama K, Uhlin U, Stubbe J. A hot oxidant, 3-NO_2Y122 radical, unmasks conformational gating in ribonucleotide reductase. J Am Chem Soc. 2010; 132:15368–15379. [PubMed: 20929229]
46. Jiang W, Xie J, Varano PT, Krebs C, Bollinger JM Jr. Two distinct mechanisms of inactivation of the class Ic ribonucleotide reductase from *Chlamydia trachomatis* by hydroxyurea: implications for the protein gating of intersubunit electron transfer. Biochemistry. 49:5340–5349. [PubMed: 20462199]
47. van Döbeln U, Reichard P. Binding of substrates to *Escherichia coli* ribonucleotide reductase. J Biol Chem. 1976; 253:3616–3622.
48. Allard P, Kuprin S, Shen B, Ehrenberg A. Binding of the competitive inhibitor dCDP to ribonucleoside-diphosphate reductase from *Escherichia coli* studied by 1H NMR. Different properties of the large protein subunit and the holoenzyme. Eur J Biochem. 1992; 280:635–642. [PubMed: 1396671]
49. Bollinger JM Jr, Tong WH, Ravi N, Huynh BH, Edmondson DE, Stubbe J. Mechanism of assembly of the tyrosyl radical-diiron(III) cofactor of *E. coli* ribonucleotide reductase. 3. kinetics of the limiting Fe^{2+} reaction by optical, EPR, and mossbauer spectroscopies. J Am Chem Soc. 1994; 116:8024–8032.
50. Baldwin J, Krebs C, Ley BA, Edmondson DE, Huynh BH, Bollinger JM Jr. Mechanism of rapid electron transfer during oxygen activation in the R2 subunit of *Escherichia coli* ribonucleotide reductase. 1. Evidence for a transient tryptophan radical. J Am Chem Soc. 2000; 122:12195–12206.
51. Solomon EI, Szilagyi RK, DeBeer George S, Basumallick L. Electronic structures of metal sites in proteins and models: contributions to function in blue copper proteins. Chem Rev. 2004; 104:419–458. [PubMed: 14871131]
52. Walsh C, Fisher J, Spencer R, Graham DW, Ashton WT, Brown JE, Brown RD, Rogers EF. Chemical and enzymatic properties of riboflavin analogues. Biochemistry. 1978; 17:1942–1951. [PubMed: 207304]

Abbreviations

α	ribonucleotide reductase large subunit
ATP	adenosine 5′-triphosphate
β	ribonucleotide reductase small subunit
C•	thiyl radical
CDP	cytidine-5′-diphosphate
DOPA	3,4-dihydroxyphenylalanine (or 3-hydroxytyrosine)
DTT	dithiothreitol
EDTA	ethylenediamine tetraacetic acid
EPL	expressed protein ligation
EPR	electron paramagnetic resonance
ET	electron transfer
F_3Y	2,3,5-trifluorotyrosine
intein wt-β2	$V_{353}G/S_{354}C$-β2 generated by EPL
k_{fwd}	forward rate constant
k_{obs}	observed rate constant
k_{rev}	reverse rate constant

NDP	nucleoside 5′-diphosphate
NH_2Y	3-aminotyrosine
NH_2Y•	3-aminotyrosyl radical
PCET	proton-coupled electron transfer
RFQ	rapid freeze quench
RNR	ribonucleotide reductase
SF	stopped-flow
TR	thioredoxin
TRR	thioredoxin reductase
W•	tryptophan radical
wt	wild-type
Y•	tyrosyl radical

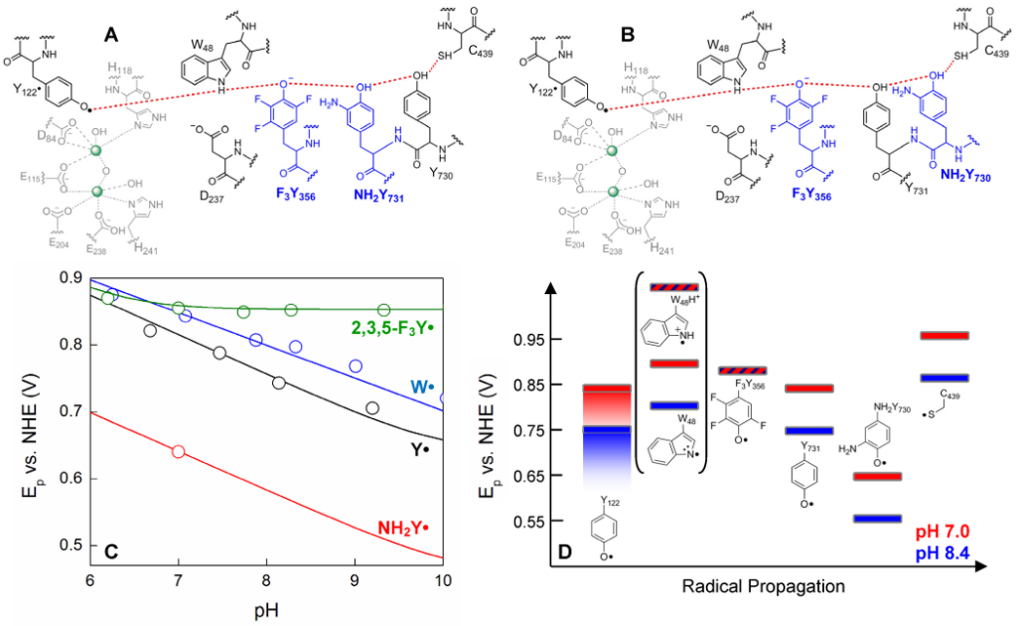

Figure 1.

The proposed radical initiation pathway and its energetics in *E. coli* RNR with site-specific incorporation of unnatural amino acids (13). Residues in grey are associated with the diferric cluster, in black are proposed pathway residues (13), and in blue are the unnatural amino acids (F_3Y and NH_2Y) to probe the pathway in the present studies. Note that the structural location of Y_{356} is unknown. (C) Peak potentials (E_p) for free (NH_2Y), and N-acetylated and C-amidated (Y, W, F_3Y) amino acids, as a function of pH. The E_ps for Y•, W• and 2,3,5-F_3Y• have been previously determined (25) and the trace for NH_2Y• has been generated from the reduction potential determined at pH 7, assuming Nernstian behavior (27). (D) The E_ps from panel (C) have been assigned to residues in the radical propagation pathway to provide a qualitative energy landscape. Red and blue rectangles represent the peak potentials for each amino acid at pH 7.0 and 8.4, respectively. The peak potentials of WH•+ and F_3Y• are represented by red rectangles with blue diagonal lines as they do not change between pH 7–8.4. The E_p range for Y_{122}• is expanded (indicated by shading), because its properties relative to the other three Ys, including its pK_a, are unique. Y_{122}• has a half-life of ~4 days and likely represents a thermodynamic hole (45). Brackets are placed around W_{48} as no direct evidence is available that places it on the pathway. If it is on the pathway, its protonation state, $W_{48}H$•+ vs. W_{48}•, that participates in radical transfer is unknown, and therefore E_ps for both of these species are included.

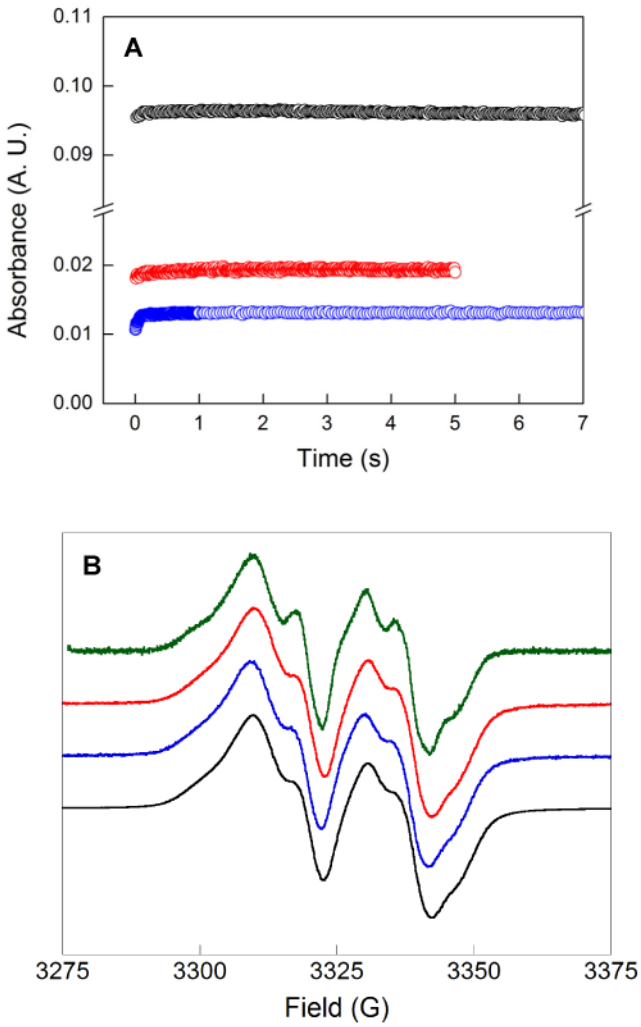

Figure 2.

SF absorption and RFQ EPR spectroscopies with F_3Y_{356}-β2 in the presence of α2 and CDP/ATP at pH 8.4. (A) Single λ SF time courses monitored at 410 nm (black), 510 nm (red) and 560 nm (blue). (B) RFQ EPR spectra of samples quenched at 72 ms (black), 138 ms (blue) and 1.9 s (red) with the EPR spectrum recorded at 77 K. The EPR spectrum of the 1.9 s quench time point was collected at 15 K (green).

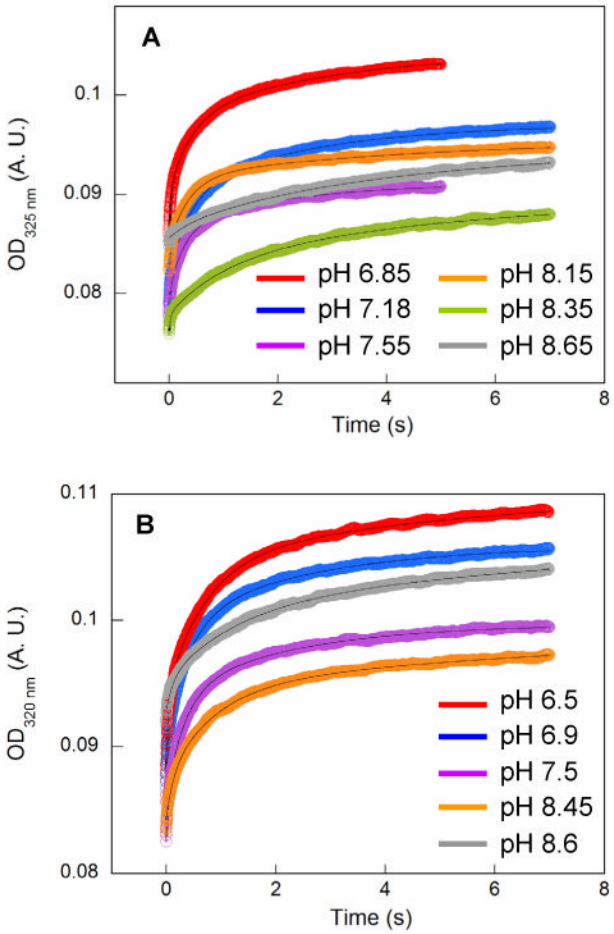

Figure 3.

SF absorption spectroscopy of NH_2Y-α2s/F_3Y_{356}-β2/CDP/ATP as a function of pH. Reaction of F_3Y_{356}-β2 with NH_2Y_{730}-α2 (A) or NH_2Y_{731}-α2 (B). Each trace is an average of 6–8 traces. Black lines describe tri-exponential fits to the data. See Table 1 for kinetic parameters.

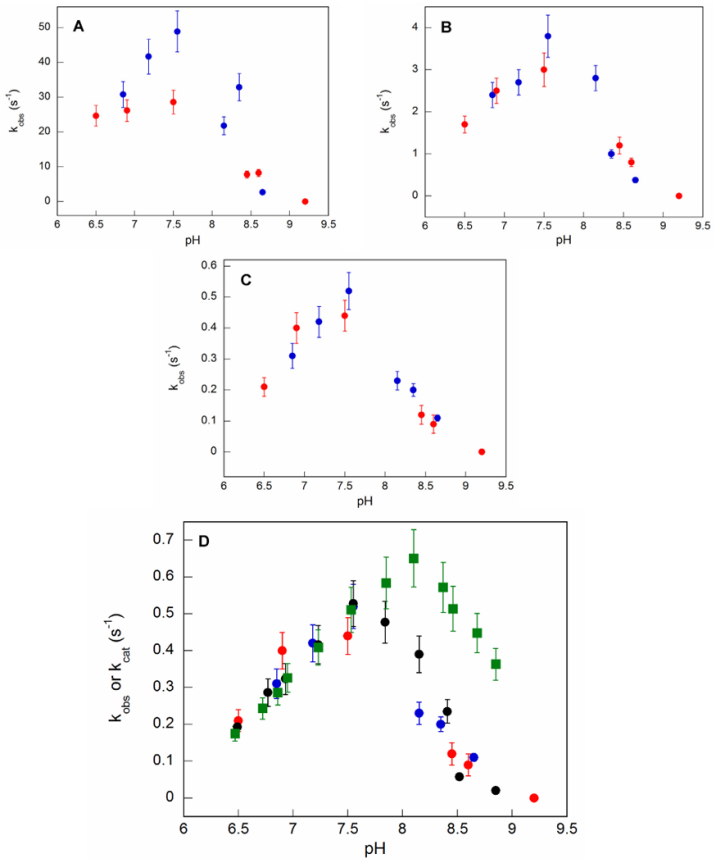

Figure 4.

pH rate profiles for NH_2Y• formation in the reactions of NH_2Y_{730}-α2 (blue dots) or NH_2Y_{731}-α2 (red dots) with F_3Y_{356}-β2 in the presence of CDP/ATP. pH dependence of the rate constants from the 1st (A), 2nd (B) and 3rd (C) kinetic phases determined from the tri-exponential fits (Table 1). In (D), the data from panel (C) are overlaid with the pH rate profiles for [^{14}C]-dCDP formation with F_3Y_{356}-β2/wt α2 (black dots) and with intein wt-β2/ wt α2 (green squares), determined in a previous study (18).

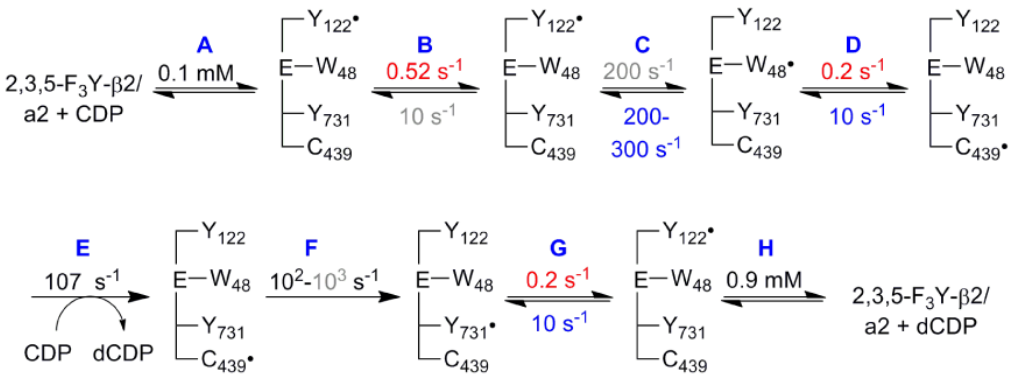

Figure 5.

Kinetic model for the catalytic cycle of F_3Y_{356}-β2 with wt α2 and CDP/ATP, which have been omitted for clarity. The K_ds and the rate constants in black have been measured experimentally (45,47,48), the rate constants in grey have been adapted from our previous simulations (36) and those in red have been measured herein and assigned to steps B, D, and G as described in the text. Rate constants in blue have been simulated herein. When assuming rate-limiting reverse PCET, step D and the intermediate prior to D were eliminated from the model, and the k_{obs} of 0.2 s^{-1} was assigned to step G. When assuming a rate-limiting forward PCET, step G and the intermediate prior to G were eliminated from the model and the k_{obs} of 0.2 s^{-1} was assigned to step D. The k_{rev} in steps C, D and G have been assigned 200-300 s^{-1}, 10 s^{-1} and 10 s^{-1}, respectively, to reproduce the lack of observable intermediates (i.e. W_{48}•).

Table 1

Summary of the kinetic parameters for $NH_2Y\bullet$ formation in the reaction of NH_2Y_{730}-α2 or NH_2Y_{731}-α2 with F_3Y_{356}-β2 and CDP/ATP.

	1st Phase		2nd Phase		3rd Phase	
pH	**k_{obs} (s^{-1}) *a***	**Amp *b* (% $Y_{122}\bullet$)**	**k_{obs} (s^{-1}) *a***	**Amp *b* (% $Y_{122}\bullet$)**	**k_{obs} (s^{-1}) *a***	**Amp *b* (% $Y_{122}\bullet$)**
			NH_2Y_{730}-α2			
6.85	30.8 ± 3.7	10 ± 1	2.4 ± 0.3	15 ± 2	0.31 ± 0.04	13 ± 2
7.18	41.7 ± 5.0	7 ± 1	2.7 ± 0.3	16 ± 2	0.42 ± 0.05	15 ± 2
7.55	48.9 ± 5.9	6 ± 1	3.8 ± 0.5	12 ± 1	0.52 ± 0.06	10 ± 1
8.15	21.8 ± 2.6	5 ± 1	2.8 ± 0.3	13 ± 2	0.23 ± 0.03	8 ± 1
8.35	32.9 ± 3.9	3 ± 1	1.0 ± 0.1	10 ± 1	0.20 ± 0.02	14 ± 2
8.65	2.7 ± 0.3	2±1	0.38 ± 0.05	9 ± 1	0.11 ± 0.01	9 ± 2
			NH_2Y_{730}-α2			
6.5	24.7 ± 3.0	11 ± 1	1.7 ± 0.2	20 ± 2	0.21 ± 0.03	13 ± 2
6.9	26.2 ± 3.1	6 ± 1	2.5 ± 0.3	18 ± 2	0.40 ± 0.05	12 ± 1
7.5	28.6 ± 3.4	6 ± 1	3.0 ± 0.4	17 ± 2	0.44 ± 0.05	11 ± 1
8.45	7.8 ± 1.0	6 ± 1	1.2 ± 0.1	14 ± 2	0.12 ± 0.02	9 ± 1
8.6	8.3 ± 1.0	5 ± 1	0.80 ± 0.1	12 ± 1	0.09 ± 0.02	13 ± 2
9.2	–	–	–	–	–	–

*a*Estimated errors based on systematic factors.

*b*The amount of $NH_2Y\bullet$ trapped has been reported as a % of total initial $Y_{122}\bullet$, which in these experiments was 4.8 μM.